

Papers

Optical Parametric Oscillator Threshold and Linewidth Studies

STEPHEN J. BROSAN AND ROBERT L. BYER, MEMBER, IEEE

(Invited Paper)

Abstract—This paper presents a detailed study of the optimum design parameters for the LiNbO_3 parametric oscillator. Theoretical and experimental studies of the optical parametric oscillator (OPO) threshold parameters and of linewidth control are presented. Consideration is given to practical factors that limit OPO performance such as laser beam quality and crystal damage mechanisms. In addition, stable single axial mode operation is reported.

I. INTRODUCTION

THE optical parametric oscillator (OPO) has been extensively studied and developed since Giordmaine and Miller first demonstrated parametric oscillation in LiNbO_3 in 1965 [1]. Following early rapid progress reviewed by Harris in 1969 [2], work in parametric oscillators has proceeded at a more deliberate pace as summarized in more recent reviews by Byer [3] and by Smith [4].

The development of large, good quality LiNbO_3 crystals [5] led to the demonstration of the Nd:YAG laser pumped 1.4–4.0 μm angle tuned LiNbO_3 OPO by Herbst *et al.* [6], in 1974. The early results were soon extended to higher output energies and narrower linewidths by Byer *et al.* [7]. These improvements led to the application of the LiNbO_3 OPO source in remote air pollution sensing [8], [9], laser induced chemistry [10], and laser isotope separation studies [11].

To date there has been no detailed study of the optimum design parameters for the LiNbO_3 OPO tunable source. This paper fills that gap by presenting theoretical and experimental studies of the OPO threshold dependencies and linewidth control. Consideration is also given to practical factors that limit the OPO performance such as laser beam mode quality and crystal damage mechanisms and limits.

Manuscript received January 2, 1979. This work was supported in part by the A.R.O., in part by the Air Force Office of Scientific Research, in part by the National Science Foundation, and in part by the Stanford Materials Research Laboratory.

R. L. Byer is with the Department of Applied Physics, Edward L. Ginzton Laboratory of Physics, Stanford University, Stanford, CA 94305.

S. J. Brosnan is with the Department of Applied Physics, Edward L. Ginzton Laboratory of Physics, Stanford University, Stanford, CA 94305. He is presently at Quanta Ray Inc., Mountain View, CA.

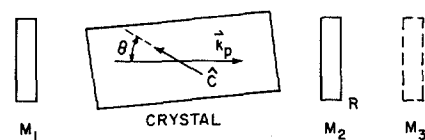


Fig. 1. Simplified OPO schematic. Mirror M_1 is highly reflecting between 1.4–2.1 μm . Output coupler M_2 has signal reflectance R . For DSRO operation, pump high reflector M_3 may be used.

A model for describing the time dependent OPO threshold pump fluence is introduced in Section II. The model and computer simulated results are compared with detailed experimental measurements of LiNbO_3 OPO threshold as a function of important parameters such as pump pulsewidth, cavity length, output coupling, and pump spatial mode parameters. The LiNbO_3 OPO operating limits and pump laser requirements are determined by crystal damage. We, therefore, present results of damage studies in Section III. In Section IV a model describing the LiNbO_3 OPO linewidth is presented. The model considers the effects of a grating, beam expander, and etalons within the OPO cavity. Using a grating with two etalons we have successfully demonstrated stable single axial mode operation of the LiNbO_3 OPO.

The theory of parametric oscillation requires an understanding of the parametric amplification process in a nonlinear medium. In an accompanying paper, Baumgartner and Byer [12] have treated optical parametric amplification (OPA) in detail. We refer to the OPA results in our theoretical treatment of the optical parametric oscillator.

II. OPO THRESHOLD

A. Theory

In this section a model is developed describing the threshold pump intensity of a pulsed singly resonant oscillator (SRO) including the effects of Poynting vector walkoff. Simplified expressions for OPO threshold are derived for the cases of a simple SRO and also for the double-pass pumped version (DSRO). A schematic of the simple oscillator is shown in Fig. 1. A more complicated resonator, which includes line narrowing elements, is easily treated in this model by general-

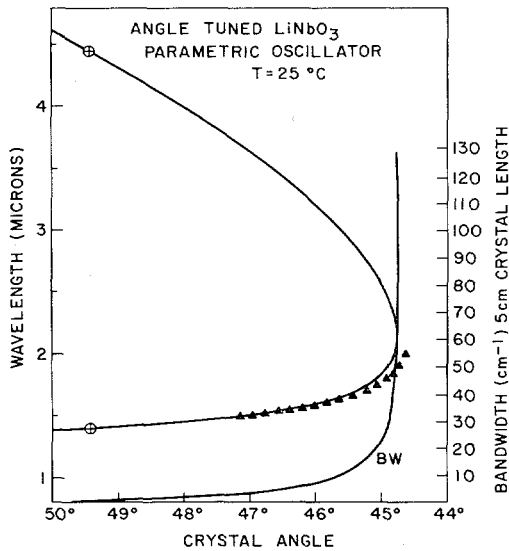


Fig. 2. Angle tuned LiNbO₃ OPO tuning curve and crystal gain bandwidth.

izing the definition of reflective cavity loss R to include all cavity discrete losses. The tuning curve of the LiNbO₃ OPO is shown in Fig. 2.

Consider a parametric oscillator with a plane-parallel two-mirror cavity. Such a configuration in a laser is unstable. Here, however, the Gaussian gain profile generated by the Gaussian pump quickly confines the resonated signal wave and stabilizes the cavity [13]. A discussion of this effect and a method for calculating signal spot size are given in Appendix A.

In the slowly varying envelope approximation the equations describing the collinear OPO fields in terms of complex phasor amplitudes, assuming no pump depletion, are given by

$$\frac{dE_s}{dz} + \alpha_s E_s = j\kappa_s E_p E_i^* e^{j\Delta k z} \quad (1)$$

$$\frac{dE_i}{dz} + \alpha_i E_i = j\kappa_i E_p E_s^* e^{j\Delta k z}$$

where the α 's are field absorption coefficients, z is the spatial coordinate in the propagation direction and $\Delta k = k_p - k_s - k_i$ defines wavevector mismatch. The interaction coefficients κ_m are defined by the following equation:

$$\kappa_m = \frac{\omega_m d_{\text{eff}}}{n_m c} \quad m = s, i \quad (2)$$

where d_{eff} is the effective nonlinear coefficient and n_m is the refractive index of the nonlinear crystal at angular frequency ω_m for the signal or idler wave.

In (1) the signal and idler fields are driven by the polarization waves possessing a spatial profile determined by the product of two field profiles. We assume that the idler wave is not resonated and is free to accept the profile of its driving polarization. The signal wave, however, is resonated. Its driving polarization must be expanded in cavity eigenmodes to find the fraction of generated signal field which is coupled into the TEM₀₀ mode of the resonator. Coupling coefficients of this type have been calculated by Kogelnik [14] and applied

to OPO's by Boyd *et al.* [15] and Asby [16]. Here, however, it is convenient to include the pump Poynting vector walkoff in the coupling coefficients for both the signal and idler waves. These coefficients and a solution to the coupled equations for the case $\alpha_s = \alpha_i = \alpha$ and $\Delta k = 0$ are given in Appendix B.

The idler field is assumed to be zero at the entrance to the crystal. The signal field at the end of a crystal of length l is given by

$$E_s(l) = E_s(0) e^{-\alpha l} \cosh \Gamma l \quad (3)$$

where

$$\Gamma = \sqrt{\kappa_s \kappa_i g_s} |E_p|^2 \quad (4)$$

is the parametric gain coefficient.

Here g_s is the signal spatial mode coupling coefficient defined in Appendix B by

$$g_s = \frac{w_p^2}{w_p^2 + w_s^2}$$

where w_p and w_s are the Gaussian mode electric field radii. An effective parametric gain length \mathcal{L} is introduced where

$$\mathcal{L} = l_w \operatorname{erf} \left(\frac{\sqrt{\pi}}{2} \frac{l}{l_w} \right) \quad (5)$$

The walkoff length l_w is given by

$$l_w = \frac{\sqrt{\pi}}{2} \frac{w_p}{\rho} \sqrt{\frac{w_p^2 + w_s^2}{w_p^2 + w_s^2/2}} \quad (6)$$

where ρ is the double refraction walkoff angle. The walkoff length is closely related to the aperture length previously introduced by Boyd *et al.* [15]. For large arguments the error function approaches unity. Therefore, the walkoff length l_w is the effective gain length for an infinitely long crystal.

The single-pass signal power gain from (3) becomes

$$\frac{|E_s(l)|^2}{|E_s(0)|^2} = e^{-2\alpha l} \cosh^2 \Gamma l \quad (7)$$

For pulsed OPO operation, the buildup to threshold may be calculated by assuming a Gaussian time profile for the incident pump intensity which yields a time dependent gain coefficient Γ described by

$$\Gamma = \Gamma_0 e^{-(t/\tau)^2} \quad (8)$$

where τ is the $1/e^2$ intensity halfwidth of the pump pulse. The generated signal wave is amplified as it makes m cavity transits from an initial parametric noise power [17]. During a single cavity transit the pump intensity is assumed to be constant, or equivalently, $\tau \gg c/n_p l$. For pass m , the signal power is, from (7),

$$P_m = P_{m-1} \{ R e^{-4\alpha l} \cosh^2 [\Gamma_0 \exp - (t_m/\tau)^2 \mathcal{L}] \} \quad (9)$$

The factor in brackets is the instantaneous cavity net gain. Equation (9) can be easily iterated numerically to compute threshold, incrementing pump intensity until a defined threshold is reached. For the calculations presented here, threshold is defined as a signal energy of 100 μJ , giving a threshold

power to noise power ratio of $\ln(P_m/P_0) = 33$. It is shown in the next section that this numerical model is in excellent agreement with experiment.

A simpler model is desirable however, for optimizing the OPO parameters that affect threshold. To allow iterative calculations we introduce a time independent gain profile of width $\bar{\tau}$ and magnitude $\bar{\Gamma}$. The width is determined by the time over which the parametric oscillator has net instantaneous gain greater than unity. From (9) we find that

$$\bar{\tau} = 2\tau \left\{ \ln \left[\frac{\Gamma_0 \mathcal{L}}{\ln(1/\sqrt{R} + \sqrt{(1/R) - 1})} \right] \right\}^{1/2} \quad (10)$$

where the relation $\cosh^{-1} x = \ln(x + \sqrt{x^2 - 1})$ has been used.

Next, we relate the square pulse height $\bar{\Gamma}$ to the Gaussian peak Γ_i . For consistency the total gain of the square pulse must equal the total gain of the Gaussian case, or

$$\frac{c\bar{\tau}}{2L} \ln \cosh^2 \bar{\Gamma} \mathcal{L} = \ln \{ \Pi_q \cosh^2 [\Gamma_0 \mathcal{L} \exp - (t_q/\tau)^2] \} \\ = \Sigma_q \ln \cosh^2 [\Gamma_0 \mathcal{L} \exp - (t_q/\tau)^2]. \quad (11)$$

For $\tau \gg 2L/c$, this summation may be approximated by an integral. If in addition the hyperbolic functions are approximated by exponentials, we obtain

$$\bar{\Gamma} \mathcal{L} = \Gamma_0 \mathcal{L} \frac{\sqrt{\pi}}{2} \left[\frac{\text{erf}(\bar{\tau}/2\tau)}{\bar{\tau}/2\tau} \right]. \quad (12)$$

Let threshold be reached after the p 'th round trip, where $p = c\bar{\tau}/2L$ with the optical cavity length L given by

$$L = L' + (n-1)l. \quad (13)$$

Here L' and l are the cavity and crystal physical lengths. Rewriting (9) in the form

$$\ln(P_n/P_0) = p \ln R - 4p\alpha l + 2p \ln \cosh \bar{\Gamma} \mathcal{L}$$

and making the exponential approximation that $\cosh \alpha = \frac{1}{2} \exp 2\alpha$ we find

$$\bar{\Gamma} \mathcal{L} = L/c\bar{\tau} \ln P_n/P_0 + 2\alpha l + \ln(1/\sqrt{R}) + \ln 2. \quad (14)$$

This equation has the clear physical interpretation of a gain equals loss threshold condition. The first term is an effective loss due to the buildup time during pulsed operation. The following terms describe distributed crystal absorption losses and the cavity output coupling loss. The final term $\ln 2$ is due to the SRO operation.

Substituting (14) into (12) we have finally

$$\Gamma_0 \mathcal{L} = 2/\sqrt{\pi} \left[\frac{\bar{\tau}/2\tau}{\text{erf}(\bar{\tau}/2\tau)} \right] \\ \cdot [L/c\bar{\tau} \ln(P_n/P_0) + 2\alpha l + \ln(1/\sqrt{R}) + \ln 2]. \quad (15)$$

Now (10) and (15) are iteratively solved for $\bar{\tau}$ and $\Gamma_0 \mathcal{L}$.

The threshold pump peak intensity using (2) and (4) and the relation $I_p = \frac{1}{2} n c \epsilon_0 |E_p|^2$ is

$$I_0 = (\Gamma_0 \mathcal{L})^2 / \kappa g_s \mathcal{L}^2 \quad (16)$$

where

$$\kappa = \frac{2\omega_s \omega_i d_{\text{eff}}^2}{n_s n_i n_p \epsilon_0 c^3}. \quad (17)$$

For LiNbO_3 we calculate in Appendix C that $d_{\text{eff}} = 5.72 \times 10^{-12}$ m/V, giving

$$\kappa = \left(9.33 \times 10^{-10} \frac{\text{cm}^2}{\text{MW}} \right) \frac{1}{\lambda_s \lambda_i} \quad (18)$$

with λ 's in cm.

The energy fluence (energy/area) threshold is calculated by integration over the temporal intensity profile and gives

$$J_0 = \sqrt{\frac{\pi}{2}} \tau I_0 = \sqrt{\frac{\pi}{2}} \tau (\Gamma_0 \mathcal{L})^2 / \kappa g_s \mathcal{L}^2 \quad (19)$$

where Γ_0 is found from an iterative solution of (10) and (15) and \mathcal{L} is given in (5).

For threshold fluence estimates one can simplify the model further by assuming $\bar{\tau}$ is fixed at 2τ , which is approximately true for most OPO configurations. With this assumption from (12) and (14) we find that $\Gamma_0 \mathcal{L} = 1.34 \bar{\Gamma} \mathcal{L}$ so that the energy fluence is directly given by

$$J_0(\bar{\tau} = 2\tau) = \frac{2.25}{\kappa g_s \mathcal{L}^2} \tau \left[\frac{L}{2\tau c} \ln \frac{P_n}{P_0} + 2\alpha l + \ln \frac{1}{\sqrt{R}} + \ln 2 \right]^2. \quad (20)$$

These are the SRO threshold fluence values for a Gaussian profile time dependent pump pulse.

A reduction in pump fluence threshold and some enhancement in OPO energy efficiency [18] may be obtained by back reflecting the pump radiation to double pass the OPO, thus creating signal gain on both the forward and backward transits of the crystal. If we let γ be the ratio of backward to forward pump field amplitude inside the crystal, then the DSRO relation analogous to (9) is

$$P_m = P_{m-1} R \exp(-4\alpha l) \cosh^2 [\Gamma_0 \mathcal{L} \exp - (t_m/\tau)^2] \\ \cdot \cosh^2 [\Gamma_0 \mathcal{L} \gamma \exp - (t_m/\tau)^2]. \quad (21)$$

If the square gain model is applied to the DSRO, the result is

$$\bar{\Gamma} \mathcal{L} = \frac{1}{1+\gamma} \left[\frac{L}{c\bar{\tau}} \ln \left(\frac{P_n}{P_0} \right) + \ln \frac{1}{\sqrt{R}} + 2\alpha l + \ln 2 \right] \quad (22)$$

where $\bar{\tau}$ is determined from

$$R \cosh^2 [\Gamma_0 \mathcal{L} \exp - (\bar{\tau}/2\tau)^2] \cosh^2 [\Gamma_0 \mathcal{L} \gamma \exp - (\bar{\tau}/2\tau)^2] = 1. \quad (23)$$

This equation is satisfied only on the wings of the gain envelope, so arguments of the hyperbolic cosines are small. In this approximation it can be shown that $\cosh \gamma x \cong (\cosh x)^{\gamma^2}$. We then obtain

$$\{ \cosh [\Gamma_0 \mathcal{L} \exp - (\bar{\tau}/2\tau)^2] \}^{1+\gamma^2} = \frac{1}{\sqrt{R}}. \quad (24)$$

Thus $\bar{\tau}$ is given by (10) with R replaced by R' ,

$$R' = (R)^{1/1+\gamma^2}. \quad (25)$$

A calculation of the DSRO relation between $\bar{\Gamma}$ and Γ_0 shows that (12) is valid for a DSRO also. We obtain for the threshold gain

$$\Gamma_0 \mathcal{L} = \frac{2}{\sqrt{\pi}} \left[\frac{\bar{\tau}/2\tau}{\text{erf}(\bar{\tau}/2\tau)} \right] \left(\frac{1}{1+\gamma} \right) \cdot \left[\frac{L}{c\bar{\tau}} \ln \left(\frac{P_n}{P_0} \right) + 2\alpha l + \ln \frac{1}{\sqrt{R}} + \ln 4 \right]. \quad (26)$$

Now (10) and (26) are solved iteratively to find $\Gamma_0 \mathcal{L}$, and threshold fluence J_0 is found from (19).

The estimated threshold fluence for $\bar{\tau} = 2\tau$ is given by

$$J_0 = \frac{2.25}{\kappa g_s \mathcal{L}^2} \frac{\tau}{(1+\gamma)^2} \left\{ \frac{L}{2c\tau} \ln \left(\frac{P_n}{P_0} \right) + 2\alpha l + \ln \frac{1}{\sqrt{R}} + \ln 4 \right\}^2. \quad (27)$$

In the model described here, an implicit assumption has been that the pump beam is collimated and has a uniform phase-front of high optical quality. For an SRO, the requirement for pump collimation is somewhat relaxed since the idler wave is free to propagate noncollinearly with phase matching being preserved. The OPO threshold is not strongly dependent upon pump collimation if the divergence cone angle is roughly less than the Poynting vector walkoff angle.

However, threshold can be markedly increased if the pump beam optical quality is nonuniform. If a transverse phase variation $d\psi/dx$ is introduced, then as the pump traverses the crystal with Poynting vector walkoff in the x direction, the generated signal wave sees a pump with a changing phase ψ_p where

$$\psi_p(z) = \left(\rho \frac{d\psi}{dx} \right) z. \quad (28)$$

From (1) we see that the transverse phase variation acts as an effective phase mismatch and reduces OPO power gain by $\text{sinc}^2 \psi_p(l)$. The critical phase variation value is set by

$$\frac{d\psi}{dx} = \frac{\pi}{\rho l}. \quad (29)$$

In a 5 cm LiNbO₃ OPO crystal the critical phase variation is approximately a quarter wave phase change per millimeter of transverse dimension. High quality lenses can easily meet this requirement, but commercial grade elements may not. In any case, near diffraction limited pump field and imaging optical components are recommended.

B. Experimental Results

In this section, the SRO theory and simplified model results are compared to experimental measurements for a 1.06 μm pumped angle tuned LiNbO₃ SRO. The pump source is an unstable resonator Nd:YAG oscillator [19] operated in the far field where the central lobe of the modified Airy disk function closely approximates a Gaussian beam. The SRO threshold energy fluence is determined as a function of cavity length, crystal length, signal wave output coupling, pump spot size, and pump pulsewidth. Agreement with theory is very good for the highest quality LiNbO₃ crystals and input pump beam profiles.

In making these measurements, a total of 26 LiNbO₃ crystals was tested over a nine month period [20]. The threshold

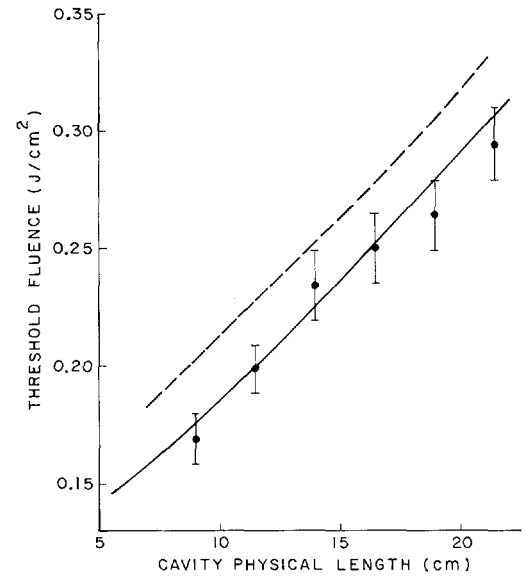


Fig. 3. SRO threshold fluence versus cavity physical length. Solid curve shows results of numerical calculation. Dashed curve shows results of square pulse model. $l = 6$ cm, $2w_p = 4$ mm, $R = 60$ percent, $\tau = 15$ ns.

energy fluence of the best crystal tested agreed very well with theory and was used to scale the experimental data to test the theory. The threshold energy fluence for an average crystal was 1.7 times greater than that of the best crystal. The standard deviation in threshold fluence for the crystals tested was 0.45. Thus the best crystal was exceptional and as yet not generally reproducible.

The Nd:YAG laser pump beam phasefront quality was another critical factor for an accurate experimental to theoretical comparison of threshold. Beam distortion in the output of some Nd:YAG lasers is severe enough to prevent OPO oscillation. In such cases propagation to the far field to allow diffraction to clean up phase perturbations may help. Beam reduction or expansion telescopes using commercial grade lenses induced enough wavefront distortion to increase the OPO threshold by 60 percent. It should be noted that the near-field phase front of the Nd:YAG laser source used in these experiments was of good quality as determined by interferometry and by the fractional conversion to the central lobe of the far-field Airy disk profile.

The simple SRO cavity configurations are shown in Fig. 1. Fig. 2 shows the LiNbO₃ angle tuning curve and the crystal gain bandwidth determined by crystal dispersion. For the theoretical-experimental comparisons discussed in this section, the simple SRO configuration was used.

Fig. 3 shows the measured SRO threshold fluence vs cavity length for a 4 mm diameter, 20 ns duration pump beam. The solid line is derived from the numerical solution of the SRO threshold condition given by (9) and is in excellent agreement with experiment. The nonlinear coefficient used for the theoretical calculation is discussed in Appendix C and yields the gain constant given by (17). The dashed line showing the simplified square pump pulse model results given by (19) is within 10 percent of the numerical results. Fig. 3 shows that the simplified threshold model is of adequate accuracy for design purposes. Its advantage lies in the ease with which it

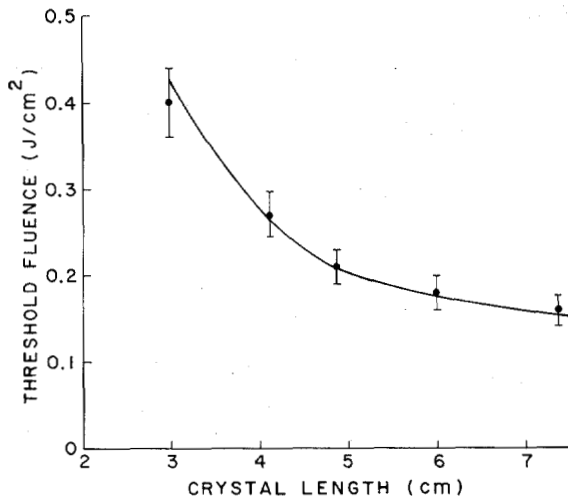


Fig. 4. SRO threshold fluence versus crystal length. $L' = 8$ cm, $2w_p = 4$ mm, $R = 60$ percent, $\tau = 15$ ns.

can be applied to OPO design calculations where a number of variables affecting threshold are considered.

The SRO threshold fluence versus LiNbO_3 crystal length is shown in Fig. 4. For these measurements a number of different crystals of comparable quality were used to minimize scatter in the measurements. The threshold values were then scaled to the value in agreement with the best 5 cm long crystal tested. The effect of pump beam Poynting vector walkoff is evident for the longest crystals tested. From the model and these measurements the optimum crystal length is approximately 5 cm.

The SRO threshold fluence dependence on signal reflectance is shown in Fig. 5. The data were taken by using a series of mirrors coated for a range of signal reflectances. However, each mirror also had a different reflectance at the pump and idler wavelengths. The data points have been individually scaled according to the DSRO to SRO ratio to reduce the variation on threshold due to pump feedback. The present model does not include the effect on SRO threshold of varying amounts of feedback at the idler field. The problem of parametric amplification with both signal and idler present was discussed in the previous paper [12]. It was shown that if the idler is present, but of the incorrect phase, the parametric gain in the crystal is effectively delayed until the phasing is corrected. The rephasing occurs by idler depletion to noise followed by regrowth at the proper phase and thus reduces the effective crystal gain length. The error brackets in Fig. 5 are an estimate of this effect.

The pump spot size dependence of parametric gain for critically phase-matched interactions is well known [15]. Fig. 6 shows the first experimental verification of the decrease in gain for small pump spot sizes as a result of Poynting vector walkoff. The model and experimental results are in good agreement and show that for a 5 cm long LiNbO_3 SRO pump, spot sizes of 4 mm diameter or greater are preferred to minimize the threshold fluence.

The model can also be applied to the OPO pumped by the near-field unstable resonator beam profile. The measured and calculated threshold fluence for the near-field pump beam

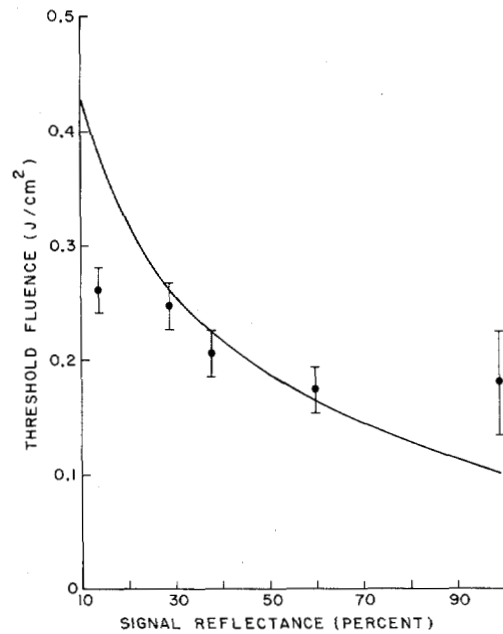


Fig. 5. SRO threshold fluence versus signal wave reflectance. Error bars reflect variations due to differing idler reflectances. $L' = 8$ cm, $l = 6$ cm, $2w_p = 4$ mm, $\tau = 15$ ns.

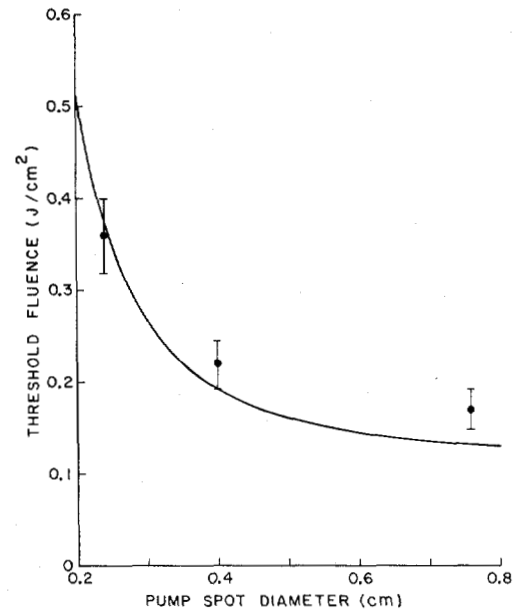


Fig. 6. SRO threshold fluence versus pump spot diameter. $L' = 8$ cm, $l = 6$ cm, $R = 60$ percent, $\tau = 15$ ns.

is 50 percent higher than that for the far field. Therefore to obtain the lowest operating OPO threshold far-field conversion of the unstable resonator mode is preferred. In the present experiments the far-field conversion was accomplished by propagating the beam for a distance of 20 m by multiple reflections between plane mirrors.

The pump pulsewidth dependence of threshold fluence is shown in Fig. 7. The pump pulsewidth was adjusted by operating the Nd:YAG oscillator at varying degrees above threshold and using a following Nd:YAG amplifier to provide the required energy. The experimental values shown in Fig. 7 are somewhat higher than theory in this case because of the pump phasefront distortion caused by the Nd:YAG amplifier

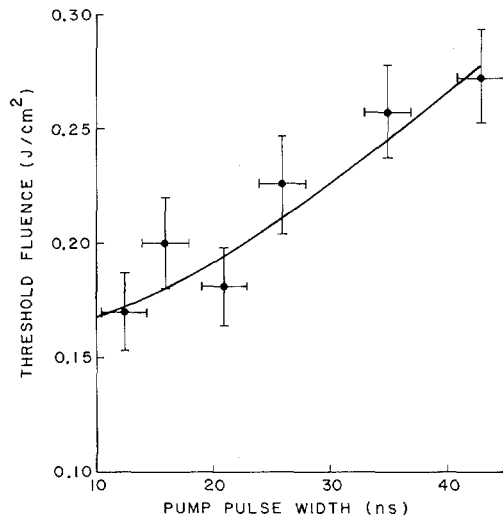


Fig. 7. SRO threshold fluence versus pump pulsewidth. Data scaled by 0.37. $L' = 8$ cm, $l = 6$ cm, $2w_s = 4$ mm, $R = 50$ percent.

crystal and also because the measurements were made in the near field. It is clear from the figure that the data, when scaled by 0.37, agree well with theory.

The results shown in Fig. 7 are for a short OPO cavity. For longer cavity lengths near 15–20 cm required to accommodate the linewidth control elements, there exists a broad threshold fluence minimum resulting in nearly constant threshold values for pulsewidths in the 10–30 ns range. For shorter pulsewidths the threshold increases due to buildup time effects. For longer pulse lengths the threshold approaches steady-state values and is constant in pump intensity.

A significant improvement in SRO performance is possible by double passing the pump beam (see Fig. 1). In addition to a threshold reduction first noted by Bjorkholm [18] and described by (26), this arrangement improves the oscillator stability, increases the conversion efficiency, and provides for separation of the tunable OPO output from the incident pump beam. With a pump high reflector mirror after the OPO output mirror, typically 60 percent of the forward propagating pump beam is reflected back into the crystal. The rest is lost to mirror and crystal surface reflections. For the present case the theoretically predicted DSRO to SRO threshold reduction is 0.54 which compares to a measured threshold reduction of 0.68 ± 0.15 .

The DSRO configuration can be simplified by coating the output mirror to reflect both the resonated signal wave and the pump wave. Coatings of this type have been designed and used in DSRO operation in spite of the more complex coating requirements.

The advantages of the DSRO configuration are not as clear cut as it appears, however. The net threshold fluence reduction is real, but the fluence at the crystal surface, which governs crystal damage is the sum of the forward and backward traveling pump waves and in fact may be larger for the DSRO at threshold than for the SRO. The double-pass pumping of the LiNbO_3 crystal also leads to a reduction in the intensity at which small-scale self-focusing occurs, thus increasing the risk of this type of damage. Finally, the reflected pump beam must be isolated from the pump laser

source to prevent the possibility of damage to the laser oscillator from excessive feedback. A pulsed Faraday rotator isolator is usually used for near-field operation of the SRO and DSRO [21]. For operation in the far field, the 20 m one-way propagation distance to the OPO provides a round-trip time delay of 120 ns which is sufficient temporal isolation. For SRO operation in the far field no feedback is observed. For DSRO operation some feedback influence is evident, but is not strong enough to affect the pump laser oscillator or the DSRO performance.

The experimental or useful conversion efficiency η , defined as the ratio of the external signal plus idler output energy to incident pump energy, is shown in Fig. 8 for the SRO. At three times threshold the observed energy conversion efficiency is 18 percent. Bjorkholm has considered the power conversion efficiency for the SRO pumped by a plane wave and Gaussian intensity beam. In his analysis an integral over the spatial mode profile of the pump wave was performed yielding a fractional transmitted pump power versus the number of times above threshold N . For pulsed OPO operation considered here, a temporal integral must also be performed to obtain the energy conversion efficiency from the peak power efficiency. The result is that the peak power conversion efficiency must be scaled by the ratio of the signal-to-pump pulsewidth, which is approximately given by $1-1/N$. Finally, to compare Bjorkholm's results to the measured conversion efficiency, the internal conversion efficiency must be scaled by the crystal surface and mirror transmittance losses. For the simple SRO cavity considered here, the scale factor is 0.6. The agreement between the theoretically expected conversion efficiency and the measured efficiency is quite good as shown in Fig. 8. The conversion efficiency of the SRO continues to increase monotonically with N as shown earlier by Byer *et al.* [7]. However, reliable operation at values of N much greater than three is difficult due to the limitations imposed by crystal damage. A more appropriate means of increasing the net OPO output energy is to increase the pump beam area but maintain operation at three times threshold for the maximum available laser energy. An alternative is to utilize an optical parametric amplifier (OPA) after the OPO as an efficient energy converter. The characteristics of the OPA as a power amplifier were discussed in the previous paper [12].

III. DAMAGE LIMITATIONS

A good understanding of the factors affecting the OPO threshold coupled with a detailed knowledge of LiNbO_3 damage mechanisms and limits is required for the design of a reliable oscillator. In this section, experimental and theoretical results are presented which describe the observed LiNbO_3 damage mechanisms. Surface damage is discussed first followed by a discussion of small-scale self-focusing which leads to internal tracking or "angel hair" damage of LiNbO_3 crystals.

The surface damage of LiNbO_3 has been extensively considered by a number of workers. In a series of papers Zverev *et al.* [22]–[24], proposed that LiNbO_3 surface damage is caused by thermal heating of an oxygen depleted niobium surface layer. In addition, the reduced niobium is assumed to be concentrated at crystal imperfections, inclusions, or

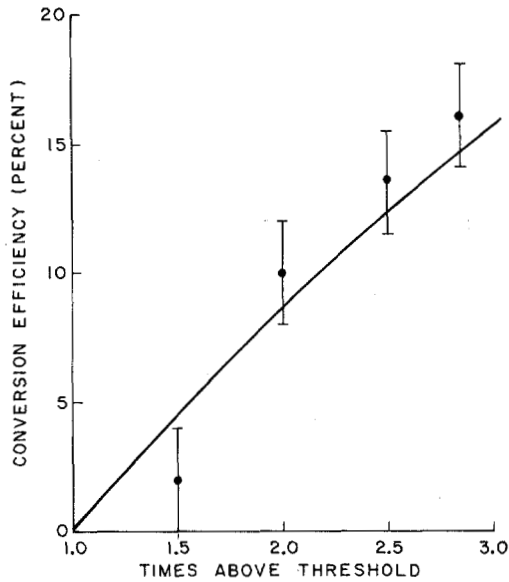


Fig. 8. SRO energy conversion efficiency versus number of times above threshold.

microcracks. Damage measurements, initially made by Zverev *et al.* and recently repeated in this laboratory, are in agreement with this basic model. Measurements of surface energy damage as a function of spot size show that the damage threshold fluence rises sharply for pump spot sizes less than 60–70 μm . The damage fluence varies from 2.7 J/cm^2 for large spot sizes to greater than 11 J/cm^2 for tightly focused spots [25]. This indicates a mean separation of surface defects on this order and is not inconsistent with the recent observation of microdomains and antidomains in LiNbO_3 and LiTaO_3 [26], [27] at this density.

The pulsewidth dependence of the damage fluence can be found by modeling the trap sites as an absorbing layer [24]. Using thermal diffusion arguments as outlined by Bliss [28] we find that for short pulses during which the layer is not completely heated the fluence limit scales as $\sqrt{\tau}$. When complete heating occurs, but pulsewidths are short compared to the thermal diffusion time into the bulk, the damage fluence is independent of τ . For longer pulses, diffusion occurs during the pulse and the damage fluence scales as τ , thereby becoming intensity limited.

Zverev [24] reports a constant fluence damage threshold of 4.6 J/cm^2 for pulsewidths less than 30 ns and a constant intensity limit of 170 MW/cm^2 for longer pulses. In an earlier paper he quotes a damage limit of 120 MW/cm^2 for a 30 ns pulse.

The results of damage measurements made in our laboratory at 1.06 μm are shown in Fig. 9(a). We measure a constant fluence damage limit of $2.7 \pm 0.4 \text{ J}/\text{cm}^2$ for uncoated LiNbO_3 in the 10–30 ns region. This value is somewhat lower than Zverev's results. For reference, Fig. 9 also shows the energy fluence just outside the surface of an *average* LiNbO_3 crystal operating at three times threshold for a short 8 cm cavity SRO. Clearly some means of raising the surface damage limit is desirable for long-term damage-free OPO operation.

The niobium ion reduction model, proposed by Zverev, provided the incentive to test the effect of oxygen on the

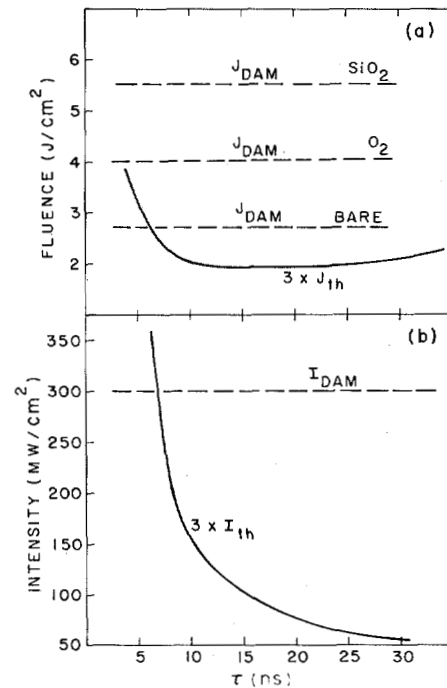


Fig. 9. Damage limits of LiNbO_3 versus pump pulsewidth. (a) Solid curve shows pump fluence at $3 \times$ OPO threshold for an *average* crystal. Surface damage fluences for the bare LiNbO_3 surface, for the uncoated surface in an O_2 atmosphere, for an SiO_2 coated crystal are shown; (b) solid curve shows pump intensity at $3 \times$ OPO threshold inside an *average* crystal. An approximate experimental self-focusing damage limit is indicated by the dashed line.

damage fluence level of LiNbO_3 [29]. The measurements were performed by mounting LiNbO_3 test plates in an oxygen atmosphere in a temperature controlled environment. Surface damage was defined as the maximum fluence at which the crystal surface did not damage when irradiated for 1 min at 10 pps by Q -switched laser pulses. All measurements were carefully normalized to a standard room temperature uncoated LiNbO_3 test plate. It has been shown that the damage fluence is strongly dependent upon the number of integrated pulses as well as pulse spatial diameter and spatial mode quality. The 1 min survival time was chosen to eliminate the dependence on integrated pulses and to be representative of actual OPO operating damage levels. The spot size was set significantly larger than the 60–70 μm defect spacing.

When oxygen was supplied to the crystal, even at room temperature, a significant increase in damage level resulted as shown in Fig. 9(a). This result was not totally unexpected since it has been known for some time that oxygen diffuses rapidly into and out of LiNbO_3 crystals and that SiO_2 anti-reflection coatings significantly increase the LiNbO_3 surface damage level as shown in Fig. 9(a). It is not clear whether the SiO_2 coating itself or the coating procedure acts to replace the LiNbO_3 surface oxygen and yield the increased damage threshold. It is known that LiNbO_3 antireflection coated with ThF_4 shows the same surface damage threshold as the uncoated crystal. The convenience of the SiO_2 coating and its antireflection reduction of surface Fresnel reflection losses to 1–2 percent clearly make it the choice for LiNbO_3 OPO operation. However, it should be kept in mind that the SiO_2 coating must be flawless since imperfections lead to phase

perturbations of the pump beam that can aggravate the onset of self-focusing.

Small-scale self-focusing using an instability theory approach is given by Suydam [31], [32]. Small spatial beam perturbations in amplitude and phase are amplified through the nonlinear intensity dependent index of refraction n_2 resulting in beam breakup and focusing.

For a Gaussian beam the critical power P_c for whole beam self-focusing is given by [33]

$$P_c = \frac{\lambda_0^2 c}{32\pi^2 n_2} \times 10^{-7} \quad (30)$$

where P_c is in watts and the other parameters are in CGS units. For small-scale self-focusing, the intensity damage limit given by Suydam is

$$I_d \left(\frac{W}{\text{cm}^2} \right) = \frac{\lambda_0 c n}{48\pi^2 n_2} \frac{\ln(3/\delta)}{z_f} (10^{-7}) \quad (31)$$

where z_f is the focusing length and δ is the depth of the small-scale perturbation. Suydam also shows that an optimum transverse spatial frequency perturbation for small-scale self-focusing exists. The spatial modulation dimension λ_m that produces the greatest self-focusing is

$$\lambda_m = \lambda \left[\frac{c 10^{-7}}{12\pi n_2 I} \right]^{1/2} \quad (32)$$

To apply small-scale self-focusing theory to LiNbO₃ we need an estimate for the magnitude of n_2 . We are unaware of any measured value for LiNbO₃ n_2 and, therefore, choose to use the approximate expression

$$n_2 (10^{-13} \text{ ESU}) = 391 \frac{n_d - 1}{v_d^{5/4}}$$

based on the empirical relation of Boling *et al.* [34]. Here v_d is the Abbé number, $v_d = (n_d - 1)/(n_f - n_c)$ where n_d and n_c are the crystal indexes of refraction at the wavelength 0.486, 0.588, and 0.656 μm . Using the above relation, we find $n_2(\text{LiNbO}_3) = 11.1 \times 10^{-13}$ ESU. This value may be an underestimate of the true value due to the effect of the d states of the niobium ion and to the application of the empirical model developed for glasses to a high index of refraction crystal.

For LiNbO₃ we find from (30) that the critical power for whole beam self-focusing is $P_c = 100$ kW. This is comparable to critical powers for materials with large values of n_2 , such as CS₂.

If we set z_f equal to the crystal length of 5 cm (10 cm for the DSRO), then for a perturbation of order $\delta = 1$ we find from (31) that $I_d = 290$ MW/cm² ($I_d = 145$ MW/cm² DSRO) for the SRO. If we take $\delta = 0.15$, as for a defect in an anti-reflection coated LiNbO₃ surface, then $I_d = 800$ MW/cm² for an SRO and 400 MW/cm² for a DSRO. The optimum transverse modulation dimension is found from (32) to be $\lambda_m = 0.5$ mm for $I = 300$ MW/cm². This dimension is approximately the spacing of crystal Schlieren defects and the Fresnel intensity modulation of a near-field unstable resonator beam.

Since n_2 for LiNbO₃ and the detailed character of the perturbations are not known, the damage values presented here are only approximate. One measured data point gave a DSRO damage track at $I_d = 300$ MW/cm². This value is shown in Fig. 9(b). Also shown in Fig. 9(b) is the intensity inside an *average* LiNbO₃ crystal operating at three times threshold for an 8 cm cavity SRO. Clearly, for pump pulses less than 10 ns duration the danger of self-focusing is critical. This is particularly the case for crystals with Schlieren defects or for beam perturbations produced by imperfect coatings or damaged optical components prior to the crystal. An additional factor may be introduced by partial mode locking or axial mode modulation in the pump beam. The resultant instantaneous intensity values may easily exceed twice the average peak intensity.

Fig. 9 clearly shows that longer pump pulsewidths reduce the OPO intensity threshold and thus reduce the probability of self-focusing. Experimentally we have found that for pulsewidths longer than 15 ns, self-focusing is avoided even in the case of severe surface damage to the crystal. The longer Q -switched pulse lengths were obtained by increasing the Nd:YAG optical cavity length. Added benefits of the longer pump pulse are a decrease in the operating linewidth of the OPO due to the increased number of passes during buildup and a greater insensitivity of intensity threshold on OPO cavity length.

In summary, Fig. 9 shows that any increase in OPO threshold brings the device closer to the surface damage or small-scale self-focusing damage limit. One may either rely on the SiO₂ antireflection coating for increased surface damage fluence or operate at a fluence less than the 2.7 J/cm² set by the bare LiNbO₃ crystal surface. In any case, care should be taken to minimize the energy fluence threshold by the proper choice of OPO parameters and by the use of a high quality pump beam of proper temporal duration.

IV. LINEWIDTH CONTROL

A. Introduction

The gain linewidth of the parametric oscillator is set by crystal dispersion [2], [3]. For the angle tuned LiNbO₃ SRO, the crystal bandwidth varies from 10 cm⁻¹ to approximately 200 cm⁻¹ at degeneracy as shown in Fig. 2. Therefore, for most applications, some linewidth reduction is desired. Theory shows that the SRO is capable of operating in a single axial mode without reduction of conversion efficiency at the resonated wave. The nonresonated wave reflects the axial mode spectrum of the pump field. Single axial mode operation has been achieved earlier for the Nd:YAG pumped noncritically phasematched LiNbO₃ SRO using a single high resolution etalon line narrowing element [35], [36].

The present angle tuned LiNbO₃ SRO requires a primary linewidth control element and an etalon for narrower linewidth operation. Primary linewidth control elements that have been tried include a thin tilted etalon, a birefringent filter, and a diffraction grating [7], [37]. The most attractive method of primary linewidth control is a grating preceded by beam expansion prisms as shown in Fig. 10. An analysis

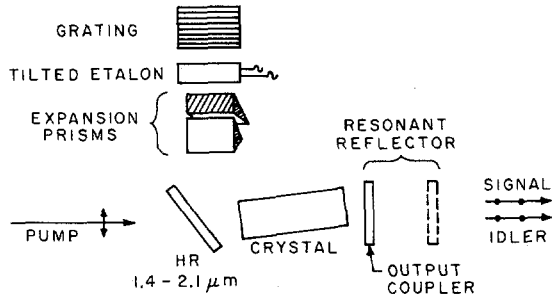


Fig. 10. Schematic of the SRO cavity for linewidth studies. Primary linewidth control is provided by prisms and grating combination. Line narrowing is accomplished with a tilted etalon. A resonant reflector used as an output coupler collapses the linewidth to a single axial mode.

of the prism expander-grating linewidth control of the OPO is presented next. In Section IV-C experimental results are described including stable single axial mode operation of the LiNbO₃ SRO.

B. Linewidth Model

In this section a model is developed that describes the SRO linewidth when operated with a resonant cavity consisting of beam expansion prisms and a grating. This method of primary linewidth control was selected because of linear tuning, a wide tuning range, and ease of implementation at a low cost.

The OPO linewidth is the result of the crystal and grating component lineshape functions after consideration for multiple passes in the optical cavity. The resultant linewidth $\Delta\nu$ is calculated from the product of the individual multiple-pass lineshapes of the crystal and of the grating. Since the lineshapes are approximately Gaussian, we may write the linewidth as

$$\frac{1}{\Delta\nu} = \sqrt{\frac{1}{[\Delta\nu_c(p)]^2} + \frac{1}{[\Delta\nu_g(p)]^2}} \quad (33)$$

where $\Delta\nu_c$ and $\Delta\nu_g$ are the crystal and grating linewidths and p is the number of cavity transits.

The lineshape function for the crystal bandwidth $\Delta\nu_c$ is given by evaluating the $\text{sinc}^2(\Delta k l/2)$ function for a phase mismatch of Δk and a crystal length of l . An analysis similar to that for the diffraction grating presented in Appendix D shows that for p passes the crystal linewidth reduces to

$$\Delta\nu_c(p) = \frac{1}{\sqrt{p}} \Delta\nu_c \quad (34)$$

where $\Delta\nu_c$ is determined by the crystal dispersion between signal and idler wavelengths and in cm^{-1} is approximately

$$\Delta\nu_c = \frac{2}{l\beta_{si}} \quad (35)$$

β_{si} is defined by

$$\beta_{si} = \left. \frac{\partial k_s}{\partial \omega} \right|_{\omega_{s0}} - \left. \frac{\partial k_i}{\partial \omega} \right|_{\omega_{i0}} \quad (36)$$

and is approximately equal to $2\Delta n_{si}$.

This basic crystal linewidth $\Delta\nu_c$ assumes a collimated pump. For divergent pump beams the linewidth increases significantly. An expansion of the wave vector mismatch for small deviations of the pump input angle and signal frequency [12] gives the linewidth increase due to pump divergence $\delta(\Delta\nu)$ of approximately

$$\delta(\Delta\nu) = \frac{2\rho\alpha}{\lambda_p \beta_{si}} \quad (37)$$

where α is the pump beam cone angle. For LiNbO₃ OPO signal and idler frequencies away from degeneracy, β_{si} is approximately 0.1. For $\rho = 0.03$ rad and $\lambda_p = 1.06 \mu\text{m}$, the linewidth broadens nearly 6 cm^{-1} per mrad of pump divergence. The crystal bandwidth is then significantly broadened by a diverging incident pump. If line narrowing elements are used, an increase in threshold may be observed because part of the generated signal wave is removed from the gain medium by cavity frequency selection.

Consider the OPO cavity shown in Fig. 10 which uses a Littrow configuration grating at resonant wavelength λ_s and grating angle θ relative to normal. For added resolution a beam expansion element of linear magnification M and angular magnification M_a is included.

The prism beam expander has been described earlier as a means of beam expansion within a dye laser cavity [38]. Klauminzer has discussed its advantages, which include ease of construction and insertion into the optical cavity [39].

Using LiNbO₃ as the prism material, we designed and constructed a two element prism expander as discussed in Appendix E. The magnification of a single prism, taken as the output to input beam width ratio W/w is given by (E-5)

$$M = \tan \theta. \quad (38)$$

For N prisms in sequence the net magnification is the product $M = M_1 M_2 M_3 \cdots M_n$ as expected.

The angular magnification of a Brewster angle prism is shown in Appendix E to be

$$\frac{1}{M_a} = \frac{\delta\theta_e}{\delta\theta_i} = \frac{1}{n} \left(\frac{1}{M} \right) = \frac{1}{M^2} \quad (39)$$

where n is the prism index of refraction. For comparison, a telescope expander has an angular magnification of

$$\frac{1}{M_a} = \frac{\delta\theta_e}{\delta\theta_i} = \frac{1}{M} \quad (40)$$

where M is the power of the telescope.

The resolution of the grating is found by differentiating the grating equation

$$m\lambda_s = d(\sin \theta_{in} + \sin \theta_{out}) \quad (41)$$

with respect to θ_{out} which yields for the Littrow case

$$\frac{d\lambda_s}{\lambda_s} = \frac{d\nu_s}{\nu_s} = \frac{d\theta}{2 \tan \theta} \quad (42)$$

Here, d is the groove spacing and m is the order number. The angular width $\Delta\theta$ is calculated in Appendix D for the case of

a multiple passed grating with an optical length $2L$ between passes. The calculation shows that diffraction not only sets the single-pass angular width but also puts a lower bound on the linewidth attainable by multiple passing. Using (D-12) we write the diffraction limited full width at half maximum (FWHM) grating linewidth as

$$\Delta\nu_g^{DL} = \frac{\sqrt{2 \ln 2}}{2 \tan \theta} \left(\frac{M}{M_a} \frac{4L\lambda_s}{\pi w_s^2} \right)^{1/3} \frac{1}{\pi M w_s} \quad (43)$$

where the factor $\sqrt{2 \ln 2}$ converts the halfwidth at $1/e^2$ linewidth to the FWHM value.

The grating resolution may be broader than that specified in (43) when the finite aperture set by the gain medium size is considered. Wave packets outside the diffraction limited bandwidth may oscillate by propagating off-angle in the cavity. These waves may experience gain over the full pump beam area. Therefore, to be consistent with the $1/e^2$ angular width used to obtain (43), we take the proper pump aperture diameter to be $2w_p$.

Consider a light ray of wavelength $\lambda_0 + \Delta\lambda$ which is initially propagating parallel to the cavity axis. It is shown in Appendix D that after its q th reflection from the grating, its angle to the axis is

$$\Delta_q = \left(\frac{M\Delta\lambda}{d \cos \theta_0} \right) q. \quad (44)$$

After a beam expansion device, this angle is $M_a\Delta_q$. If we note that the gain region establishes an effective aperture of width equal to the pump spot diameter $2w_p$, then the number of passes p in which the ray travels across the aperture is determined by

$$2w_p = 2DM_a\Delta_1 \sum_{q=1}^p q \quad (45)$$

where the sum has the value $p(p+1)/2$ and D is an effective cavity length. In air, D would simply be the physical cavity length. Here, however, the presence of a crystal of index n_s and a beam expansion device of angular expansion $M_a(M^2$ for prisms, M for a telescope) gives

$$D = l_c/n_s + l_a + l_{ex}/M_a \quad (46)$$

where the crystal, air, and expander lengths are given by l_c , l_a , and l_{ex} , respectively. In practice, p is fixed by the cavity buildup time. The contribution to grating linewidth due to cavity geometry is then

$$\Delta\nu_{cav} = \sqrt{2 \ln 2} \frac{2w_p \cos \theta}{mp(p+1)D\lambda_s^2 M_a}. \quad (47)$$

The full grating linewidth is thus a sum of the diffraction and aperture width terms given by

$$\Delta\nu_g(p) = \sqrt{2 \ln 2} \left[\frac{1}{2 \tan \theta} \left(\frac{M}{M_a} \frac{4L\lambda_s}{\pi w_s^2} \right)^{1/3} \frac{1}{\pi M w_s} + \frac{2w_s d \cos \theta}{mp(p+1)M_a D \lambda_s^2} \right]. \quad (48)$$

We now consider the relative magnitudes of the diffraction and aperture width terms in (48) for typical cavity configurations in an effort to understand which parameters are important to the design of a narrow-band OPO. If we let $w_p = 0.2$ cm, $w_s = 0.06$ cm, $\lambda_s = 1.7$ μ m, $1/d = 6000$ lines/cm, $D = 8$ cm, and $m = 1$, we find that for a 10 ns pump pulse and no expansion, the inclusion of the aperture term increases the linewidth by 30 percent. For a 20 ns long pump pulse the aperture term contribution to the linewidth is reduced by multiple passing to 8 percent. If beam expansion prisms are used, the effect of the aperture term becomes negligible. From (48) it is clear that to improve linewidth performance we may increase grating θ and/or increase the beam diameter on the grating, $2Mw_s$. However, each approach has limits. As θ increases, the free spectral range of the grating decreases and does not allow OPO operation over the full tuning range from 1.4 to 2.1 μ m. Increasing M requires a four prism beam expander and a larger grating and has the disadvantage of increasing threshold due to the added cavity length. However, for sufficiently long pump pulsewidths near 20 ns the increase in threshold may be tolerable.

Various techniques exist for additional linewidth control. Single frequency operation using interferometer arrangements have been demonstrated for lasers [40] and for parametric oscillators [35]. Internal tilted etalons have also been used successfully [41], but have suffered from insertion losses, a problem which is alleviated by the use of beam expansion prisms. Due to their ease of alignment we have chosen to use tilted etalons to attain narrow-band operation.

The lineshape function $f_e(\Delta\nu)$ for a transmitted beam of a tilted etalon is Lorentzian in the frequency deviation from resonance, $\Delta\nu = \nu - \nu_0$, for $\Delta\nu \ll \nu_0$,

$$f_E(\Delta\nu) = [1 + 4\mathcal{F}^2(\Delta\nu)^2/(\Delta\nu_{FSR})^2]^{-1} \quad (49)$$

where \mathcal{F} is the etalon finesse and $\Delta\nu_{FSR}$ is the free spectral range $2nt$ for a material of thickness t and index n . For p passes through the etalon, the linewidth reduces to

$$\Delta\nu_E(p) = \frac{\Delta\nu_E(1)}{\sqrt{p}}. \quad (50)$$

Clearly, (33) could be extended by adding $[\Delta\nu_E(p)]^{-2}$ to the sum of linewidth factors under the square root.

For the present application as an internal cavity element with short optical pulses, various loss mechanisms arise. The insertion loss γ for a tilted etalon in a CW laser cavity has been treated by Leeb [42] and found to be

$$\gamma_E = \frac{2R}{(1-R)^2} \left(\frac{2t\theta_E}{nw_0} \right)^2 \quad (51)$$

where R is the power reflectivity, θ_E is the tilt angle, and w_0 is the spot size in the direction perpendicular to the rotation axis. When the prism expander is used, w_0 is large and $\gamma_E < 10$ percent even for an $\mathcal{F} = 20$ etalon.

A more important loss mechanism for short pulse applications is due to the delay propagation time through the etalon as considered by Daussy *et al.* [43]. They find that a delay near 1 ns may occur for high finesse etalons. This can amount

to a considerable loss during the buildup time, increasing OPO threshold prohibitively. Another finding is that the effective pulsed finesse may be significantly ($\sim \frac{1}{3}$) lower than that calculated for a steady-state condition. These results are consistent with our experimental linewidth results for the pulsed LiNbO_3 OPO operating with a tilted etalon line-narrowing element.

C. Experimental Results

The linewidths for a number of OPO cavity configurations (see Appendix F), have been measured and compared with theory. In general the agreement is good. The observed discrepancies can often be attributed to factors such as crystal quality or optical alignment. As in the threshold measurements described in Section II, we have found that crystal optical uniformity is an important factor and that the presence of Schlieren variations in the index of refraction of a crystal increase the measured linewidth up to a factor of two.

Optical alignment of the cavity and of pump beam collimation telescopes is also more important for narrow linewidths than for threshold minimization. Some care must be exercised in the centering of the grating resonance upon the peak of the crystal bandwidth. A lineshape asymmetry caused by a broadening of the high frequency side of the line occurs if this condition is violated. If the grating is tuned off line center, the crystal phase-matching condition is broken more slowly on the high frequency side, since the OPO waves may then angle phase match and propagate noncollinearly. On the low frequency side, $\Delta k > 0$ so that the OPO waves remain collinear but are reduced in magnitude. The amount of broadening may be calculated by expanding the wave vector mismatch allowing for angle phase matching and is found to be quadratic in the angle between signal and pump beams. For minimum linewidths and collinear beams it is then recommended that the grating be tuned slightly to the low frequency side of the crystal bandwidth.

The measured and calculated linewidths for OPO cavities with increasing spectral selectivity are given in Table I. The first block of entries shows that a prism power of 10 is required to give wavelength control to the grating. The resulting grating linewidth is 0.53 cm^{-1} . A typical linewidth trace taken using a scanning 1 m spectrometer is shown in Fig. 11.

It is experimentally observed that the OPO output beam at 2-3 times threshold has the same spot size as the incident pump beam. This is explained by noting that the confinement of the signal beam is relaxed as the peak of the pump is depleted, and the signal spot size may increase to approach the incident pump spot size. It might be argued that the proper w_s to use in (48) is this larger spot. However, the linewidth is determined during buildup before depletion occurs and is, therefore, set by the smaller confined signal spot size as calculated in Appendix A.

If a tilted etalon is inserted into the cavity, the OPO linewidth is reduced as shown in the second group of entries in Table I. As a rule of thumb, the etalon free spectral range is chosen to be twice the grating linewidth. A single etalon mode is then produced with the linewidth determined by the

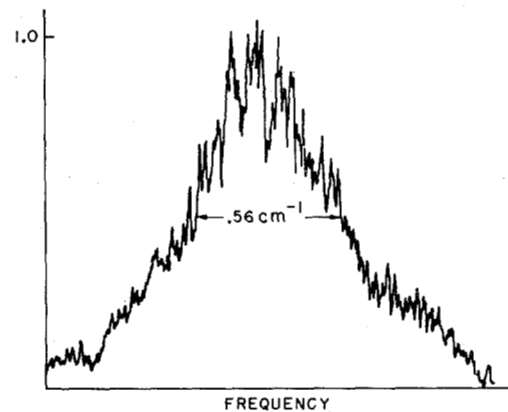


Fig. 11. SRO grating linewidth using a ten power prism beam expander as measured using a scanning 1 m spectrometer.

TABLE I
OPO LINewidths: THEORY AND EXPERIMENT PARAMETERS: $\lambda_s = 1.6 \mu\text{m}$,
 $w_p = 0.2 \text{ cm}$, $\tau_p = 10 \text{ ns}$, $L = 20 \text{ cm}$, $D = 8 \text{ cm}$, $N = 6000 \text{ lines/cm}$

Configuration	Linewidth (cm^{-1})		Comments
	Theory	Expt	
Grating only	2.2	2.2	$w_p = .15 \text{ cm}$ Crystal has wavelength control
Grating, x5 prisms	.86	.73-1.2	Grating & crystal both control
Grating, x10 prisms	.40	.53	Grating has λ control
Grating, x5 prisms + 2 mm, $F = 7$ etalons	.059	< .1	2 etalon modes
+ 1 mm, $F = 7$ etalons	.15	.14	1 etalon mode
+ .5 mm, $F = 7$ etalons	.3	.63	1 etalon mode
Grating, x10 prisms 2 mm, $F = 7$ etalons	.02	.075	20 ns pump pulse 3 axial modes FWHM
Grating, x10 prisms 2 mm, $F = 7$ etalons Reflective etalon ($R = 50\%$, 60%)		< .02	Single axial mode operation - very stable

effective multipass finesse. As discussed above, the insertion loss of the etalon increases with increasing F imposing a limit on the linewidth attainable with a single etalon. We have found experimentally that for a finesse greater than 10, the insertion loss raises the OPO threshold excessively, even when the etalon is used in the prism expanded beam.

In a final series of measurements, we have improved the line-narrowed OPO performance and have successfully demonstrated stable single axial mode operation. An elliptical 20 ns pump beam was incident with a 6 mm major diameter oriented in the walkoff plane to minimize threshold and a 2 mm minor diameter set as the aperture for grating narrowing. A reflective etalon was added to the cavity in the form of a pair of output coupler mirrors spaced 5 cm apart. In this experiment, the nonoptimum choice of 50 and 60 percent reflecting mirrors was used. The output linewidth was analyzed by diverging the OPO output through an air spaced plane parallel

Fabry-Perot etalon with a finesse of 20 in the visible. The resulting rings were observed with an infrared vidicon and photographed from the monitor display. With the output reflective etalon mirror misaligned, the etalon ring pattern shown in Fig. 12(a) was obtained. The pattern shows that the OPO operated at an FWHM linewidth of 0.075 cm^{-1} , or three axial modes spaced 0.025 cm^{-1} apart. When the outside mirror was aligned to form a reflecting etalon, the linewidth collapsed to a single axial mode, as shown in Fig. 12(b). The etalon effect of the output mirror pair was verified by observing the frequency jumps of 0.1 cm^{-1} by tilting the lower resolution etalon angle. The single axial mode frequency was quite stable and repeatable which is noteworthy since no special experimental precautions were taken to establish an interferometrically stable OPO cavity. Also, due to the 1 s persistence time of the vidicon, observation of clear axial modes supports the claim of their frequency stability. The OPO is a reactive device with small thermal loading of the LiNbO_3 crystal and optical cavity thus avoiding resonator instabilities. To the resolution limit of the analyzer etalon the FWHM of a single axial mode appears to be less than 0.01 cm^{-1} or 300 MHz. The expected Fourier transform limited bandwidth is near 100 MHz. The measured output pulse energy in single-mode operation was 10 mJ, which is approximately 80 percent of the un-narrowed OPO output energy under similar pumping conditions.

V. CONCLUSION

This paper summarizes the parameters relevant to the design of a reliable LiNbO_3 parametric oscillator capable of stable narrow-band operation. The prime requirements involve the quality of both the LiNbO_3 crystal and the pump laser beam.

Imperfect crystal quality is a major cause of increases in both the OPO threshold and linewidth. The oscillation threshold for an average LiNbO_3 crystal is 70 percent higher than that predicted for an ideal crystal. Linewidths may be increased by a factor of two in crystals with Schlieren defects. Pump laser phasefront quality is also important and high quality optical components are essential. For example, the use of commercial grade lenses in a telescope may increase the threshold by 60 percent.

The operating limits of the OPO are set by the onset of crystal damage. There are two types of damage, and each imposes a constraint upon the configuration of the pump beam. Internal crystal tracking due to small-scale self-focusing scales as the peak power of the pump pulse. Pulse lengths greater than 10 ns are essential to avoid self-focusing, and pulses longer than 15 ns are highly recommended. In addition, the surface of LiNbO_3 may be damaged by a peak energy fluence of 2.7 J/cm^2 for uncoated LiNbO_3 . The damage limit is somewhat higher for an SiO_2 antireflection coated surface.

We have designed the LiNbO_3 OPO for a minimum threshold fluence to provide for reliable damage free operation. The threshold increase due to pump beam walkoff leads to a minimum pump spot diameter of 4 mm and crystal length

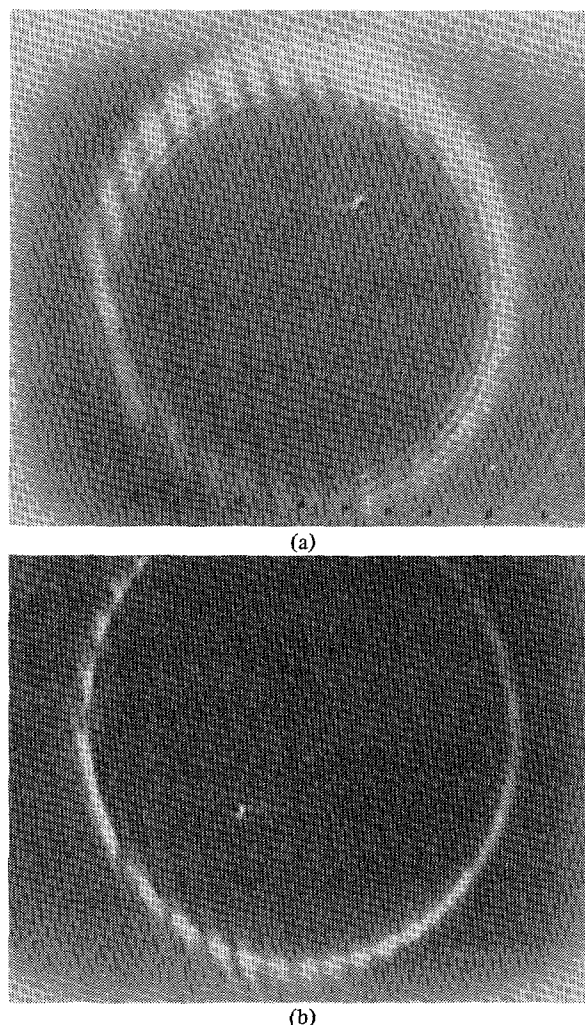


Fig. 12. SRO linewidth measurements using Fabry-Perot etalon. OPO cavity includes a tilted etalon and resonant reflector: (a) resonant reflector is misaligned, producing an FWHM linewidth of 0.075 cm^{-1} , or 3 axial modes; (b) resonant reflector is aligned, producing stable single axial mode operation.

of 5–6 cm. In addition the cavity length should be minimized. A complete cavity, including grating, prism ten-power expander and tilted etalon may be constructed with a 16 cm physical length. Since the effective loss due to buildup time dominates other loss mechanisms, the threshold is not a strong function of output coupler reflectivity R . For greater useful energy conversion, it is necessary that the output coupler provide the dominant cavity loss. Therefore, we choose to operate with an output reflectivity of less than 50 percent.

The required pump energy to operate the LiNbO_3 SRO varies with crystal and pump laser, but lies in the 100–150 mJ range. As an added note, we have operated a considerable number of OPO cavity configurations as summarized in Appendix F. However, the best results to date have been obtained with the “L” cavity which utilizes the input beam splitter as shown in Fig. 10.

Narrow linewidths have been achieved in the LiNbO_3 OPO with the use of a 600 l/mm diffraction grating in first order with the addition of a 10× prism beam expander. The measured linewidths were 0.5 cm^{-1} . A 2 mm tilted etalon with

$\mathcal{F} = 7$ reduces this linewidth to 0.08 cm^{-1} , corresponding to operation with 3 axial modes. A reflective etalon output coupler configuration further collapses the output to a single axial mode which is remarkably stable in frequency.

The angle tuned LiNbO_3 parametric oscillator is a useful laboratory tool for studies which require a broadly tunable source of narrow-band infrared radiation.

APPENDIX A RESONATED WAVE SPOT SIZE

For a Gaussian profile gain medium, the signal spot size evolves during buildup to threshold to a radius determined by the pump spot size and diffraction. We calculate in this appendix the resonated signal wave steady-state spot size and determine whether this condition is indeed reached during the OPO buildup time. We proceed by considering the signal spot size as it is iteratively narrowed by the gain polarization and broadened by diffraction. The balance determines the final signal wave spot size.

Let the fields have Gaussian profiles

$$E_j = E_{j0} \exp -r^2/w_j^2. \quad (\text{A-1})$$

From (1) we see that the driving polarization for the OPO waves have radii \bar{w}_i given by

$$\frac{1}{\bar{w}_s^2} = \frac{1}{w_i^2} + \frac{1}{w_p^2}, \quad \frac{1}{\bar{w}_i^2} = \frac{1}{w_s^2} + \frac{1}{w_p^2}. \quad (\text{A-2})$$

The idler wave is free and therefore, assumes the profile of its driving polarization, or $\bar{w}_i = w_i$. The signal polarization radius may now be written as

$$\frac{1}{\bar{w}_s^2} = \frac{1}{w_s^2} + \frac{2}{w_p^2}. \quad (\text{A-3})$$

The radius of this wave when allowed to propagate a cavity round trip is

$$\bar{w}_s'^2 = \bar{w}_s^2 \left[1 + \left(\frac{2L\lambda}{\pi \bar{w}_s^2} \right)^2 \right]. \quad (\text{A-4})$$

We let $\bar{w}_s' = w_s$ and iterate to see how soon a stable signal mode radius is established. Numerical iteration shows that a spot size within 30 percent of steady state is established in only 2-3 cavity round trips. This verifies the assumption made in the model.

The steady-state signal spot size is found directly by again letting $\bar{w}_s' = w_s$ and substituting (A-4) into (A-3). The resulting condition is a cubic equation in \bar{w}^2

$$\left(\frac{\pi}{2L\lambda} \right)^2 \bar{w}_s^6 + \bar{w}_s^2 - \frac{w_p^2}{2} = 0. \quad (\text{A-5})$$

From this calculation we find that the signal spot size is significantly less than that of the pump. For example, a pump spot of 2 mm radius incident on a 15 cm long OPO cavity operating at $1.9 \mu\text{m}$ produces a signal spot size of 0.62 mm. This spot size is important for later linewidth calculations.

Some experimental evidence exists to support the prediction for a small confined signal spot size. In an initial experiment to measure OPO threshold, a 6 mm diameter pump beam was

apertured to a diameter of 2 mm with no change in threshold. This showed that near threshold only the central portion of the pump is useful in providing signal gain. Next, the flat OPO cavity output mirror was replaced by a curved mirror to produce a Gaussian mode stable cavity with a signal spot size equal to that predicted by the confined signal calculation above. No change in OPO threshold was observed lending support to the model presented here.

It should be noted that for higher pump powers, the Gaussian profile assumed in this calculation becomes flattened and distorted due to depletion. This relaxes the constraint on the signal spot size which may expand to match that of the pump. However, the spot size calculated here should be valid during the OPO buildup time and at operation near threshold.

APPENDIX B SRO-SINGLE PASS GAIN SOLUTION INCLUDING POYNTING VECTOR WALKOFF

To calculate the signal and idler field buildup in an OPO resonator, some care must be taken to consider only that fraction of the generated signal wave which couples into the resonator. In addition, the coupling of the pump and generated waves is gradually broken due to pump wave Poynting vector walkoff. If is convenient to treat both effects in the coupling coefficient formalism of Kogelnik [14].

The radii of the polarization fields for the signal and idler waves \bar{w}_s and \bar{w}_i are found in Appendix A to be

$$\bar{w}_i = w_i, \quad \bar{w}_s = [1/w_s^2 + 2/w_p^2]^{-1/2}. \quad (\text{B-1})$$

Because the signal wave is resonant its polarization profile must be expanded in terms of cavity modes.

Only the TEM_{00} mode is of interest here. Let P_j represent the Gaussian profile of a polarization which drives the signal or idler wave. If we describe the fields in transverse coordinates x and y , the coupling coefficient can be written as

$$c_{00} = \left[\int_{-\infty}^{\infty} P_j(x) E_j^*(x) dx \right] \left[\int_{-\infty}^{\infty} P_j(y) E_j^*(y) dy \right] \quad (\text{B-2})$$

where $E_j(x)$ and $E_j(y)$ are normalized. Including walkoff the signal coupling coefficient is

$$c_{00}^s = \frac{2}{\pi w_s^2} \left[\int_{-\infty}^{\infty} dx \exp \left\{ -x^2 \left(\frac{2}{w_s^2} + \frac{1}{w_p^2} \right) - \frac{(x - \rho z)^2}{w_p^2} \right\} \right] \cdot \left[\int_{-\infty}^{\infty} dy \exp \left\{ -y^2 \left[\frac{2}{w_s^2} + \frac{2}{w_p^2} \right] \right\} \right] \quad (\text{B-3})$$

where ρ is the walkoff angle. Integration yields,

$$c_{00}^s = g_s \exp - \left[\frac{\pi}{4} \left(\frac{z}{l_w} \right)^2 \right] \quad (\text{B-4})$$

where

$$l_w = \frac{\sqrt{\pi}}{2} \frac{w_p}{\rho} \sqrt{\frac{w_p^2 + w_s^2}{w_p^2 + w_s^2/2}} \quad (\text{B-5})$$

and

$$g_s = \frac{w_p^2}{w_p^2 + w_s^2} \quad (\text{B-6})$$

For the idler, the result is,

$$c_{00}^i = \exp \left[-\frac{\pi}{4} \left(\frac{z}{l_w} \right)^2 \right]. \quad (\text{B-7})$$

The polarization terms of (1) can now be rewritten in terms of cavity mode field

$$\frac{dE_s}{dz} + \alpha_s E_s = j\kappa_s g_s E_p E_i^* \exp \left(-\frac{\pi}{4} \frac{z^2}{l_w^2} \right) e^{j\Delta kz} \quad (\text{B-8})$$

$$\frac{dE_i}{dz} + \alpha_i E_i = j\kappa_i E_p E_s^* \exp \left(-\frac{\pi}{4} \frac{z^2}{l_w^2} \right) e^{j\Delta kz}. \quad (\text{B-9})$$

Let

$$E_s = E'_s e^{-\alpha_s z}, \quad E_i = E'_i e^{-\alpha_i z}. \quad (\text{B-10})$$

Then

$$\begin{aligned} \frac{dE'_s}{dz} &= j\kappa_s g_s E_p E_i'^* \exp \left(-\frac{\pi}{4} \frac{z^2}{l_w^2} \right) e^{j\Delta kz} \\ \frac{dE_i'^*}{dz} &= j\kappa_i E_p^* E'_s \exp \left(-\frac{\pi}{4} \frac{z^2}{l_w^2} \right) e^{-j\Delta kz} \end{aligned} \quad (\text{B-11})$$

where $\alpha_s = \alpha_i \equiv \alpha$ is assumed. Let $\Delta k = 0$, since we are interested in a phase-matched OPO. Then substitution yields

$$\frac{d}{dz} \left[\exp \left(\frac{\pi}{4} \frac{z^2}{l_w^2} \right) \frac{d}{dz} \right] E'_s = \kappa_s \kappa_i g_s |E_p|^2 \left[\exp - \left(\frac{\pi}{4} \frac{z^2}{l_w^2} \right) \right] E'_s. \quad (\text{B-12})$$

Changing variables by letting

$$z' = \int_0^z \exp -\frac{\pi}{4} \frac{z''^2}{l_w^2} dz'' \quad (\text{B-13})$$

yields

$$\frac{d^2 E'_s}{dz'^2} = \kappa_s \kappa_i g_s |E_p|^2 E'_s. \quad (\text{B-14})$$

The solution satisfying the boundary condition that $E'_s = E_s(0)$ and $E'_i = 0$ at $z' = 0$ is

$$E_s(z) = E_s(0) e^{-\alpha_s z} \cosh \Gamma z' \quad (\text{B-15})$$

where

$$\Gamma = \sqrt{\kappa_s \kappa_i I_p} \quad (\text{B-16})$$

with κ and I_p defined by

$$\kappa = \frac{2\omega_s \omega_i d_{\text{eff}}^2}{n_s n_i n_p \epsilon_0 c^3}, \quad I_p = \frac{1}{2} n c \epsilon_0 |E_p|^2.$$

The idler wave has the solution

$$E_i(z) = E_s(0) e^{-\alpha_i z} \sqrt{\frac{\kappa_i}{g_i \kappa_s}} e^{-1/2j(\psi_p + 3\pi)} \sinh \Gamma z' \quad (\text{B-17})$$

where ψ_p is the phase of the pump field.

APPENDIX C

EFFECTIVE NONLINEAR COEFFICIENT FOR LiNbO₃

For LiNbO₃ with a point group symmetry of $\bar{3}m$, the effective nonlinear coefficient is [44]

$$d_{\text{eff}} = d_{31} \sin \theta - d_{22} \cos \theta \quad (\text{C-1})$$

where θ is the angle between the optic axis and pump propagation direction. Also, $d_{22} = -0.53 d_{31}$ [45]. So for $\theta = 47^\circ$, in the middle of the OPO tuning range, we have

$$d_{\text{eff}} = 1.09 d_{31}. \quad (\text{C-2})$$

From 1.06 μm second-harmonic generation measurements the recommended value of d_{31} given by Choy [46] is 5.95×10^{-12} m/V. We scale this to the OPO wavelength range, by using the dispersionless Miller's Delta Δ_{ijk} value of 1.13×10^{-3} , where

$$\Delta_{ijk} = \frac{d_{ijk}}{\epsilon_0 (n_s^2 - 1) (n_i^2 - 1) (n_p^2 - 1)}. \quad (\text{C-3})$$

Using the measured indexes of refraction for congruent LiNbO₃ [47] we find

$$d_{\text{eff}} = 5.72 \times 10^{-12} \text{ m/V}. \quad (\text{C-4})$$

APPENDIX D

MULTIPLE PASS DIFFRACTION GRATING RESOLUTION

In this Appendix we consider the multiple passed reflection of monochromatic light from a defraction grating and calculate the resulting angular halfwidth for the case in which a propagation length $2L$ is allowed between grating reflection. This distance permits diffraction to again broaden the grating-narrowed divergence angle and to establish a steady-state $\Delta\theta_D$ independent of further grating reflections.

Neglect for the present the effect of L and consider the normalized grating intensity function for infinitely narrow grooves as given by [48]

$$\bar{I} = \frac{\sin^2 \aleph \gamma}{\aleph^2 \sin^2 \gamma} \quad (\text{D-1})$$

where \aleph is the number of illuminated grating grooves and γ is defined by

$$\gamma = \frac{\pi d}{\lambda} [\sin \theta_0 + \sin (\theta_0 + \Delta\theta)]. \quad (\text{D-2})$$

Here d is the groove spacing, θ_0 is the incident angle relative to grating normal, and $\Delta\theta$ is the deviation of a reflected light ray from Littrow configuration. The grating resonance is defined by

$$\frac{2\pi d}{\lambda} \sin \theta_0 = n\pi \quad (\text{D-3})$$

where n is an integer. If $\Delta\theta \ll 1$, we then find that

$$\gamma = \frac{\pi d}{\lambda} \cos \theta_0 \Delta\theta. \quad (\text{D-4})$$

After p reflections the grating intensity function becomes

$$\bar{I}(p) = \left[\frac{\sin^2 \pi \gamma}{(\pi \gamma)^2} \right]^p \quad (\text{D-5})$$

We define the angular halfwidth of the grating to be the angular deviation from resonance $\Delta\theta_D$ which reduces the grating intensity function to $1/e^2$ of its maximum. A numerical calculation using (D-5) shows that to a good approximation

$$\pi \gamma = \frac{2}{\sqrt{p}} \quad (\text{D-6})$$

for $p \gg 1$. The angular halfwidth of a grating narrowed light packet is then, from (D-4) and (D-6),

$$\Delta\theta_D = (\lambda/\pi W) 1/\sqrt{p} \quad (\text{D-7})$$

where W is the $1/e^2$ spot radius and $\aleph = 2W/d$ has been used. The far field diffraction limited divergence angle is then reduced by $1/\sqrt{p}$ for a multipassed grating.

The propagation length $2L$ is now included to calculate the effect of diffraction. For a Gaussian beam, the divergence angle $\theta_{1/2}$ is $w(z)/R(z)$ where $w(z)$ is the spot size and $R(z)$ is the beam curvature [49]. We have then

$$\theta_{1/2} = \frac{\lambda}{\pi w_0} \sqrt{1 + \left(\frac{z_R}{z}\right)^2} \quad (\text{D-8})$$

where z_R is the Rayleigh range $\pi w_0^2/\lambda$. If beam expansion prisms are used, this angle is reduced by $1/M_a$. Since $w_s = W_s/M$ we obtain

$$\theta_{1/2} = \frac{\lambda}{\pi W_s} \frac{M}{M_a} \sqrt{1 + \left(\frac{z_R}{2L}\right)^2} \quad (\text{D-9})$$

We are interested in the steady-state condition which must occur for some p' . We may approximately write

$$\frac{\lambda}{\pi W_s} \left[\frac{1}{\sqrt{p'+1}} + \frac{M/M_a}{\sqrt{1+(z_R/2L)^2}} \right] = \frac{\lambda}{\pi W_s} \frac{1}{\sqrt{p'}} \quad (\text{D-10})$$

where L is the cavity optical length. Assuming $p' > 1$ yields

$$4p'^2(p'+1) \cong \left(\frac{M_a}{M}\right)^2 \left[1 + \left(\frac{z_R}{2L}\right)^2 \right]. \quad (\text{D-11})$$

Therefore

$$p' \cong \left(\frac{M_a}{M} \frac{z_R}{4L}\right)^{2/3} \quad (\text{D-12})$$

If (D-11) is less than unity we set $p' = 1$. For $w_s = 0.6$ mm, $\lambda_s = 1.9$ μ m, $L = 15$ cm, and $5 \times$ prisms, $p' = 3$. This is much less than the transits possible during the OPO buildup time $c\tau/2L$. Thus the same diffractive process which stabilizes the spot size evolution in Appendix A is also responsible for the rapid stabilization of the diffraction limited half-width to the steady-state value

$$\Delta\theta_D = \left(\frac{M}{M_a} \frac{4L\lambda}{\pi w_s^2}\right)^{1/3} \frac{\lambda_s}{\pi W_s} \quad (\text{D-13})$$

We also need to understand the mechanism of the ejection of off-resonant wavelengths from a grating mirror cavity of

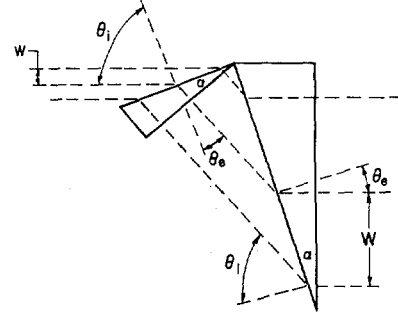


Fig. 13. Two prism expander setup. Incident and exit angles are shown as θ_i and θ_e . Prisms apex angle is a α . Magnification is given by W/w .

center wavelength λ_s and grating angle θ_0 . If $\lambda = \lambda_0 + \Delta\lambda$, the grating equation becomes

$$\sin \theta' + \sin \theta'' = \frac{m\lambda}{d} \quad (\text{D-14})$$

where d is the groove spacing, and for pass n

$$\theta' = \theta_0 - \Delta_{n-1}, \quad \theta'' = \theta_0 + \Delta_n$$

where θ' and θ'' are the incident and exit angles relative to the grating normal. Expansion of (D-13) yields

$$\Delta_n = \Delta_{n-1} + \frac{mN(\Delta\lambda)}{\cos \theta_0} \quad (\text{D-15})$$

For the resonant wavelength λ_0 , the grating acts as a simple mirror. For a wavelength deviation $\Delta\lambda$, the grating reflection angle, relative to the cavity axis, is incremented by $m\aleph\Delta\lambda/d \cos \theta$ on each pass. If we take $\Delta_0 = 0$,

$$\Delta_n = \left(\frac{m\aleph\Delta\lambda}{d \cos \theta_0}\right) n. \quad (\text{D-16})$$

APPENDIX E

BREWSTER ANGLE BEAM EXPANSION PRISMS

Consider the two prism beam expanders shown in Fig. 13. The linear magnification of a single prism is given by

$$M = \frac{\cos \theta_e}{\cos \theta_i} \quad (\text{E-1})$$

where θ_i and θ_e are the angles of incidence and exit from the prism first surface. The maximum magnification occurs when the beam exits normal to the prism second surface. Then $\theta_e = \alpha$, where α is the prism apex angle and Snell's law results in

$$M = \frac{1}{n} \frac{\tan \theta_i}{\tan \alpha} \quad (\text{E-2})$$

For low insertion loss the incident angle is set at Brewster's angle so that

$$n = \tan \theta_i \quad (\text{E-3})$$

and

$$M = \frac{1}{\tan \alpha} = n. \quad (\text{E-4})$$

Therefore, near Brewster's angle

$$M \cong \tan \theta_i. \quad (\text{E-5})$$

The angular magnification for a prism beam expander is found by differentiating Snell's law

$$\delta \theta_i \cos \theta_i = n \cos \theta_e \delta \theta_e \quad (\text{E-6})$$

so that

$$\frac{\delta \theta_e}{\delta \theta_i} = \frac{1}{n} \frac{\cos \theta_i}{\cos \theta_e}. \quad (\text{E-7})$$

Using (E-1) and (E-4), we have for a Brewster angle prism

$$\frac{1}{M_a} = \frac{\delta \theta_e}{\delta \theta_i} = \frac{1}{nM} \cong \frac{1}{n^2}. \quad (\text{E-8})$$

Therefore,

$$M_a = Mn \cong M^2. \quad (\text{E-9})$$

For comparison, a telescope has an angular magnification of

$$M_a = M. \quad (\text{E-10})$$

The minimum optical path length l_0 through a prism is given by

$$l_0 = nW \tan \alpha \cong W. \quad (\text{E-11})$$

The two prism expander is nearly achromatic. The angular deviation $\Delta \theta$ for an index dispersion Δn is to first order

$$\Delta \theta = (1/n_0 - 1/n_0^2) \Delta n \quad (\text{E-12})$$

where n_0 is the mean index of refraction of the medium. For glass prisms, the angular deviation is only 2.7 mrad over the entire visible spectrum.

The insertion loss of the prisms is given by the Fresnel reflection loss at the first surface plus the antireflection coating loss at the near normal surface. For the LiNbO_3 prisms, this loss is less than 1 percent per prism, which is insignificant compared to output coupling losses. Thus the LiNbO_3 prisms beam expander is readily inserted into the OPO cavity without significantly increasing threshold.

APPENDIX F

EXPERIMENTAL CAVITY CONFIGURATIONS

In the course of this work, a number of OPO configurations have been constructed in an effort to reduce threshold and to improve linewidth performance. We have found that the Gaussian pump profile is necessary for minimum threshold due to the longer walkoff length. Attempts to improve performance have concentrated on a reduction of cavity length, as shown by the in-line arrangements using Fresnel pump coupling [Fig. 14(a)] and using a dichroic input/output separation mirror [Fig. 14(b)]. The latter is necessarily a DSRO but has the disadvantage that for moderate pump levels the signal wave feedback from the pump high reflector mirror is sufficient for oscillation. In the Fresnel coupled cavity, the pump is reflected off the first prism surface. This arrangement works well but is somewhat inconvenient to align and does not

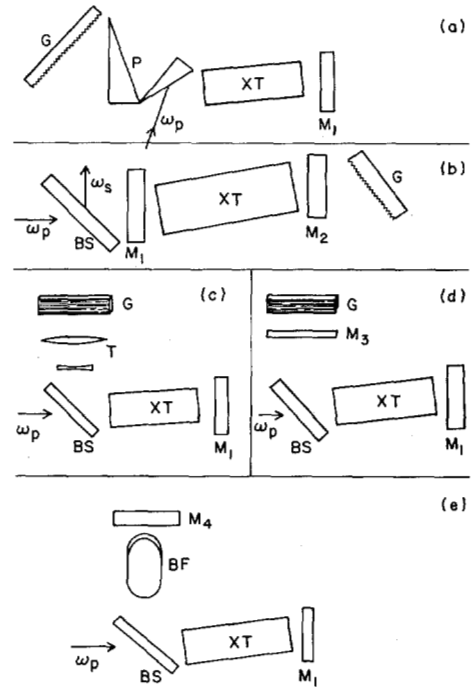


Fig. 14. OPO cavity configurations: (a) pump input coupling using Fresnel reflection of prisms P ; (b) M_2 is pump high reflector, dichroic beam splitter BS is used to separate signal output; (c) telescope T used for beam expansion; (d) partially reflecting signal mirror M_3 to act with grating G as resonant reflector; (e) birefringent filter BF used as line-narrowing element, M_4 is signal high reflector. Other elements: crystal = XT , output coupler = M_1 .

efficiently couple the pump beam into the cavity. The L -shaped cavity using a dichroic input mirror shown in Fig. 10 performs better than any other configuration we have tested.

For linewidth control we have operated cavities with a Galilean telescope expander [Fig. 14(c)], a mirror/grating combination rear reflector [Fig. 14(d)] and a Brewster angle birefringent tuning element [Fig. 14(e)]. The telescope expander is difficult to align and to collimate. It also suffers from chromatic aberration and produces back reflected focal spots which may damage other components. The resonant mirror/grating setup must be interferometrically stable to operate properly. Birefringent tuning has the disadvantage of being nonlinear. We find that the diffraction grating when preceded by a prism beam expander has better performance than any other configuration tested.

ACKNOWLEDGMENT

We want to acknowledge the contributions of R. A. Baumgartner during the early part of this work.

REFERENCES

- [1] J. A. Giordmaine and R. C. Miller, "Tunable coherent parametric oscillation in LiNbO_3 at optical frequencies," *Phys. Rev. Lett.*, vol. 14, pp. 973-976, 1965.
- [2] S. E. Harris, "Tunable optical parametric oscillators," *Proc. IEEE*, vol. 57, pp. 2096-2113, 1969.
- [3] R. L. Byer, "Optical parametric oscillators," in *Treatise in Quantum Electronics*, H. Rabin and C. L. Tang, Eds. New York: Academic, 1973, pp. 587-702.
- [4] R. G. Smith, "Optical parametric oscillators," in *Lasers*, A. K.

- Levine and A. J. DeMaria, Eds. New York: Dekker, 1976, pp. 189-307.
- [5] R. L. Byer, R. L. Herbst, R. S. Feigelson, and W. L. Kway, "Growth and application of (01.4) LiNbO_3 ," *Opt. Commun.*, vol. 12, pp. 427-429, 1974.
- [6] R. L. Herbst, R. N. Fleming, and R. L. Byer, "A 1.4-4.0 μm high energy angle tuned LiNbO_3 parametric oscillator," *Appl. Phys. Lett.*, vol. 25, pp. 520-522, 1974.
- [7] R. L. Byer, R. L. Herbst, R. N. Fleming, "A broadly tunable IR source," in *Proc. Second Int. Conf. on Laser Spectroscopy*, Megeve, France, 1975. Berlin: Springer, 1975, pp. 206-226.
- [8] T. Henningsen, M. Garbuny, and R. L. Byer, "Remote detection of CO by parametric tunable laser," *Appl. Phys. Lett.*, vol. 24, pp. 242-244, 1974.
- [9] R. A. Baumgartner and R. L. Byer, "Remote SO_2 measurements at 4 μm with a continuously tunable source," *Opt. Lett.*, vol. 2, pp. 163-165, 1978.
- [10] A. Kung and C. B. Moore, to be published.
- [11] A. Kaldor, R. Rabinowitz, D. M. Cox, J. A. Horsley, and R. Brickman, "Laser chemistry experiments with UF_6 ," presented as invited paper at the 10th Int. Quantum Electronics Conference, Atlanta, GA, June 1978.
- [12] R. A. Baumgartner and R. L. Byer, "Optical parametric amplification," this issue, pp. 432-444.
- [13] L. W. Casperson and S. D. Lunnam, "Gaussian modes in high loss laser resonators," *Appl. Opt.*, vol. 14, pp. 1193-1199, 1975.
- [14] H. Kogelnik, "Coupling and conversion coefficients for optical modes," in *Proc. Symp. on Quasi-Optics*, vol. 14. Brooklyn, New York: Polytechnic, 1964, pp. 333-347.
- [15] G. D. Boyd and A. Ashkin, "Theory of parametric oscillator threshold with single mode optical masers and observation of amplification in LiNbO_3 ," *Phys. Rev.*, vol. 146, p. 198, 1966.
- [16] R. Ashby, "Optical mode interaction in nonlinear media," *Phys. Rev.*, vol. 187, pp. 1062-1069, 1969.
- [17] R. L. Byer and S. E. Harris, "Power and bandwidth of spontaneous parametric emission," *Phys. Rev.*, vol. 168, pp. 1064-1068, 1968.
- [18] J. E. Bjorkholm, "Some effects of spatially nonuniform pumping in pulsed optical parametric oscillators," *IEEE J. Quantum Electron.*, vol. QE-7, pp. 109-118, 1971.
- [19] R. L. Herbst, H. Komine, and R. L. Byer, "A 200 mJ unstable resonator Nd:YAG oscillator," *Opt. Commun.*, vol. 21, pp. 5-7, 1977.
- [20] The crystals tested were from the Stanford Center for Materials Research and from Crystal Technology, Inc., Mountain View, CA.
- [21] R. L. Byer, "Parametric oscillators" in *Tunable Lasers and Applications*, A Mooradian, T. Jasper, and P. Stokseth, Eds. Berlin: Springer, 1976, pp. 76-80.
- [22] G. M. Zverev, E. A. Levchuk, V. A. Pashkov, and Yu. P. Poryadin, "Laser-radiation-induced damage to the surface of lithium niobate and tantalate," *Sov. J. Quantum Electron.*, vol. 2, pp. 167-169, 1972.
- [23] —, "Damage to the surface of lithium niobate by light," *Sov. Phys. JETP*, vol. 35, pp. 165-167, 1972.
- [24] G. M. Zverev, S. A. Kolyadin, E. A. Levchuk, and L. A. Skvortsov, "Influence of the surface layer on the optical strength of lithium niobate," *Sov. J. Quantum Electron.*, vol. 7, pp. 1071-1075, 1977.
- [25] M. M. Choy, private communication.
- [26] J. D. Venables, "Damage-induced microdomains in LiTaO_3 ," *Appl. Phys. Lett.*, vol. 25, pp. 254-256, 1974.
- [27] N. Ohnishi and T. Iizuka, "Etching study of microdomains in LiNbO_3 single crystals," *J. Appl. Phys.*, vol. 46, pp. 1063-1067, 1975.
- [28] E. S. Bliss, "Pulse duration dependence of laser damage mechanisms," *Opto-Electronics*, vol. 3, pp. 99-108, 1971.
- [29] Measurement initially done by T. Henningsen, private communication and later repeated in this laboratory by M. Endemann as described in text.
- [30] R. W. Wallace, private communication.
- [31] B. R. Suydam, "Self-focusing of very powerful laser beams," in *Laser Induced Damage in Optical Materials*, A. J. Glass and A. H. Guenther, Eds. Washington, DC: NBS Special Publ. 387, 1973, pp. 42-48.
- [32] B. R. Suydam, "Self-focusing of very powerful laser beams, II," *IEEE J. Quantum Electron.*, vol. QE-10, pp. 837-843, 1974.
- [33] E. L. Kerr, "Filamentary tracks formed in transparent optical glass by laser beam self-focusing. II, Theoretical analysis," *Phys. Rev. A*, vol. 4, pp. 1195-1218, 1971.
- [34] N. L. Boling, A. J. Glass, and A. Owyong, "Empirical relationships for predicting nonlinear refractive index changes in optical solids," *IEEE J. Quantum Electron.*, vol. QE-14, pp. 601-608, 1978.
- [35] J. Pinard and J. F. Young, "Interferometric stabilization of an optical parametric oscillator," *Opt. Commun.*, vol. 4, pp. 425-427, 1972.
- [36] R. W. Wallace, Chromatix Inc., private communication.
- [37] R. L. Byer and R. L. Herbst, "Parametric oscillation and mixing," in *Nonlinear Infrared Generation*, Y. R. Shen, Ed. Berlin: Springer, 1977, pp. 81-137.
- [38] S. A. Myers, "An improved line narrowing technique for a dye laser excited by a nitrogen laser," *Opt. Commun.*, vol. 14, pp. 187-9, 1971. Also in D. C. Hanna, P. A. Karkhainen, and R. Wyatt, "A simple beam expander for frequency narrowing of dye lasers," *Opt. Quantum Electron.*, vol. 7, pp. 115-119, 1975.
- [39] G. K. Klauminzer, "New high performance short cavity dye laser design," presented as a Post-Deadline Paper at Conf. on Laser Engineering and Applications, Washington, DC: 1977.
- [40] P. W. Smith, "Stabilized, single-frequency output from a long laser cavity," *IEEE J. Quantum Electron.*, vol. QE-1, pp. 343-348, 1965.
- [41] M. Hercher, "Tunable single mode operation of gas lasers using intracavity tilted etalons," *Appl. Opt.*, vol. 8, pp. 1103-1106, 1969.
- [42] W. R. Leeb, "Losses introduced by tilting intracavity etalons," *Appl. Phys.*, vol. 6, pp. 267-272, 1975.
- [43] H. Daussy, R. Dumanchin, and O. deWitte, "Fabry-Perot with short pulse laser: Spectral selection and spectral analysis in dye lasers," *Appl. Opt.*, vol. 17, pp. 451-458, 1978.
- [44] J. F. Midwinter and J. Warner, "The effects of phase matching method and of uniaxial crystal symmetry on the polar distribution of second order nonlinear optical polarization," *Brit. J. Appl. Phys.*, vol. 16, pp. 1135-1142, 1965. Orientation is chosen so $\Phi = 90^\circ$.
- [45] G. D. Boyd, R. C. Miller, K. Nassau, W. L. Bond, and A. Savage, " LiNbO_3 : An efficient phase-matched nonlinear optical material," *Appl. Phys. Lett.*, vol. 5, pp. 234-236, 1964.
- [46] M. M. Choy and R. L. Byer, "Accurate second order susceptibility measurements of visible and infrared nonlinear crystals," *Phys. Rev. B*, vol. 14, pp. 1693-1706, 1976.
- [47] D. S. Smith, H. D. Riccius, and R. P. Edwin, "Refractive indices of lithium niobate," *Opt. Commun.*, vol. 17, pp. 332-335, 1976.
- [48] M. Born and E. Wolf, *Principles of Optics*, 4th ed. New York: Pergamon, 1970, p. 404.
- [49] H. Kogelnik and T. Li, "Laser beams and resonators," *Proc. IEEE*, vol. 54, pp. 1312-1329, 1966.